

# Topologically protected, correlated end spin formation in carbon nanotubes

Cătălin Pașcu Moca,<sup>1,2</sup> Wataru Izumida,<sup>3</sup> Balázs Dóra,<sup>4</sup> Örs Legeza,<sup>5</sup> János K. Asbóth,<sup>6</sup> and Gergely Zaránd<sup>1,6</sup>

<sup>1</sup>MTA-BME Quantum Dynamics and Correlations Research Group, Institute of Physics, Budapest University of Technology and Economics, Budafoki út 8., H-1111 Budapest, Hungary

<sup>2</sup>Department of Physics, University of Oradea, 410087, Oradea, Romania

<sup>3</sup>Department of Physics, Tohoku University, Sendai 980-8578, Japan

<sup>4</sup>Department of Theoretical Physics and MTA-BME Lendület Topology and Correlation Research Group, Budapest University of Technology and Economics, 1521 Budapest, Hungary

<sup>5</sup>Strongly Correlated Systems Lendület Research Group, Institute for Solid State Physics and Optics, Wigner Research Centre for Physics, P.O. Box 49, H-1525 Budapest, Hungary

<sup>6</sup>BME-MTA Exotic Quantum Phases 'Lendület' Research Group, Institute of Physics, Budapest University of Technology and Economics, Budafoki út 8., H-1111 Budapest, Hungary

(Dated: February 12, 2021)

For most chiralities, semiconducting nanotubes display topologically protected end states of multiple degeneracies. We demonstrate using density matrix renormalization group based quantum chemistry tools that the presence of Coulomb interactions induces the formation of robust end spins. These are the close analogues of ferromagnetic edge states emerging in graphene nanoribbons. The interaction between the two ends is sensitive to the length of the nanotube, its dielectric constant, as well as the size of the end spins: for  $S = 1/2$  end spins their interaction is antiferromagnetic, while for  $S > 1/2$  it changes from antiferromagnetic to ferromagnetic as the nanotube length increases. The interaction between end spins can be controlled by changing the dielectric constant of the environment, thereby providing a possible platform for two-spin quantum manipulations.

*Introduction* – Topological insulators represent unique states of matter, and besides their theoretical appeal, they hold promise for revolutionizing quantum computation, spintronics and thermal electronics [1–3]. While their insulating bulk does not differ significantly from that of a simple band insulator, their topological character is manifested by the appearance of emergent surface and edge states, frequently exhibiting unusual physical properties. Probably the best known incarnation of a topological state is the edge state in the Su-Schrieffer-Heeger (SSH) model [4], describing the dimerization of polyacetylene. In this case, the dimerized phase is a topological band insulator, and correspondingly, at the edges of the polyacetylene chain or at topological defects separating different dimerized phases, mid-gap bound states and corresponding local spin excitations emerge [5, 6].

Although nanotubes have continuously been in the focus of extremely intense research for more than two decades by now [7–16], surprisingly, it has been discovered only recently that most insulating carbon nanotubes also belong to the class of topological systems. As a consequence, they should possess mid-gap states [17–19], quite similar to those found in the SSH model. Quite astonishingly, as we discuss below, the number and character of these mid-gap states is exclusively determined by the chirality of the nanotube, and in most nanotubes, several end states are predicted to appear at each end of the tube. However, in a neutral and non-interacting nanotube, all these states would be almost degenerate, and therefore they are expected to be most sensitive to interaction effects.

In this work, we focus our attention to these interac-

tion effects, and demonstrate that — in the presence of interactions — these topologically protected end states behave in many ways as spontaneously formed quantum dots. In particular, interactions lead to spin formation and tend to align spins ferromagnetically at each end of the nanotube [20–23], thereby producing end spins of size

$$S_1 = S_2 = \frac{N_{\text{edge}}}{2}, \quad (1)$$

with  $N_{\text{edge}}$  denoting the total number of topologically

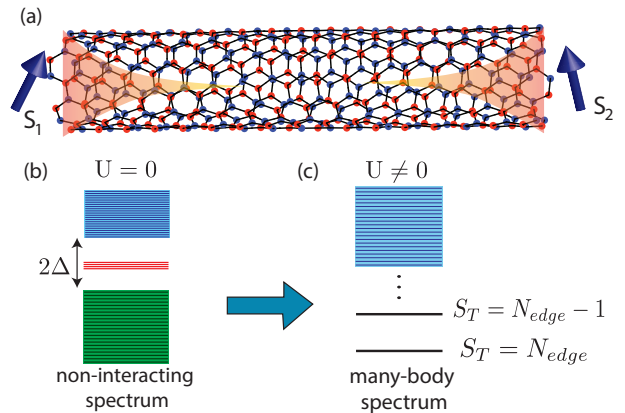


FIG. 1. (a) Topologically protected spins are formed at both edges of most semiconducting nanotubes. (b) Band structure of a semiconducting nanotube in the absence of interactions. Topological end states (red lines) appear in the gap. (c) Many-body spectrum at finite interaction. For ferromagnetic end spin coupling, the ground state has a total spin  $S_T$ , equal to the number of edge states  $N_{\text{edge}}$ . Spin excitations appear at low energies due to coupling between end spins.

protected mid-gap states at each end (see Fig. 1.(a)). Depending on chirality,  $N_{\text{edge}}$  can be quite large for many nanotubes, implying the appearance of surprisingly large end spins, paralleling in many ways ferromagnetic edge states observed in graphene nanoribbons [24–29]. The two end spins then couple to each other via an exchange interaction which, in the absence of spin-orbit coupling, takes on a simple form:

$$H_{\text{exch}} = \frac{1}{2} J_{\text{eff}} \mathbf{S}_1 \mathbf{S}_2. \quad (2)$$

The sign and strength of the exchange interaction here turns out to depend sensitively on the length of the nanotube as well as on its chirality and the dielectric constant of its environment. Spin-orbit coupling is not expected to influence spin formation, it will, however, lead to some degree of exchange anisotropy, and also induce local spin anisotropies. As a result, the SU(2) degenerate spin multiplets are expected to split, and for long nanotubes the end  $S > \frac{1}{2}$  spins will behave rather as coupled Ising spins.

*Hamiltonian.* – In this work, we use a tight binding approach to describe interacting nanotubes [30], and express the Hamiltonian as

$$H = - \sum_s \sum_{\mathbf{r}, \mathbf{r}'} t(\mathbf{r} - \mathbf{r}') c_s^\dagger(\mathbf{r}) c_s(\mathbf{r}') + \frac{1}{2} \sum_{\mathbf{r}, \mathbf{r}'} V(\mathbf{r} - \mathbf{r}') : n(\mathbf{r}) :: n(\mathbf{r}') :. \quad (3)$$

Here  $c_s^\dagger(\mathbf{r})$  creates an electron with spin  $s$  at the  $p_z$  orbital of a carbon atom at a position  $\mathbf{r}$ . The hopping matrix elements  $t(\mathbf{r} - \mathbf{r}')$  describe hopping between nearest neighbour and next nearest neighbour orbitals. They incorporate curvature effects [31], and also can be generalized to include spin-orbit effects neglected here [32]. The second term in Eq. (3) accounts for the long-ranged Coulomb interaction between local charge fluctuations on the nanotube

$$V(\mathbf{r}) = \frac{e^2}{\epsilon} \frac{1}{\sqrt{\mathbf{r}^2 + \alpha^2}}, \quad (4)$$

with  $U_0 = 11.3 \text{ eV}$  and  $\alpha \approx 0.127 \text{ nm}/\epsilon$  a short distance cut-off, and  $\epsilon$  the dielectric constant [33]. Densities in Eq. (3) appear in a normal ordered form,  $: n(\mathbf{r}) : \equiv \sum_s (c_s^\dagger(\mathbf{r}) c_s(\mathbf{r}) - 1/2)$ , thereby measuring deviations from half filling. In the following, we shall determine and analyze the many-body ground state and excitation spectrum of this Hamiltonian.

*Non-interacting nanotubes and topological end states.*— Nanotubes are classified by their chirality,  $\chi = (n, m)$ , i.e. the lattice vector  $\mathbf{C} = n\mathbf{a}_1 + m\mathbf{a}_2$ , along which a graphene sheet needs to be rolled up to form the nanotube. In this work, we focus on semiconducting nanotubes with  $(n - m) \bmod 3 = \pm 1$ .

For topological considerations, it is most useful to consider a perfect and infinite nanotube, and use a so-called

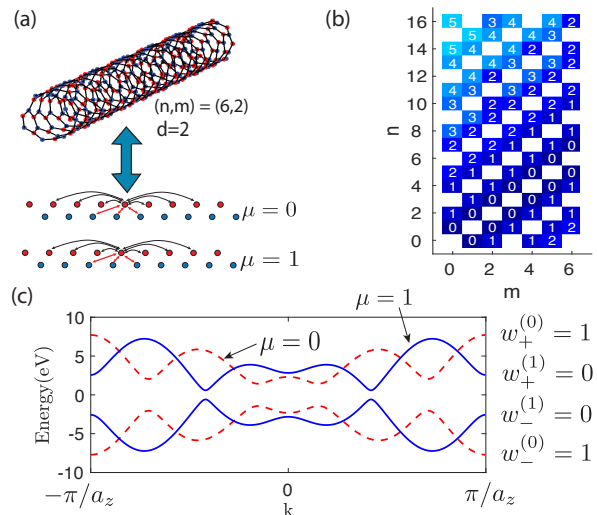


FIG. 2. (a) Mapping of an infinite carbon nanotube to an effective 1D ladder-like lattice model with  $d$  decoupled chains, for a chirality  $\chi = (n, m)$  and  $d = 2$ . Arrows indicate hoppings between carbon atoms. (b) The number of edge states,  $N_{\text{edge}}$ , as a function of the chirality  $\chi = (n, m)$ . (c) Band structure and the corresponding winding numbers for a (6, 2) nanotube.

helical construction [34, 35]. Similar to graphene, the nanotube possesses two sublattices,  $A$  and  $B$ . In the helical construction, one introduces a helical vector  $\mathbf{H}$  within the graphene sheet, and lines up all atoms of the nanotube along just  $d$  spirals along the direction  $\mathbf{H}$ , with  $d$  defined as the greatest common divisor of  $n$  and  $m$  (see supplemental material [36] for details).

Clearly, an infinite nanotube possesses a discrete  $d$ -fold rotational symmetry around the axis of the tube,  $C_d$ , and a 'gliding' (helical) translational symmetry along the chain, as generated by the helical vector  $\mathbf{H}$ . Correspondingly, single particle (but also many-body) states can be labeled by their 'angular momentum'  $\mu = 0, \dots, d-1$  and a quasimomentum  $k$  along the chain, and are organized into  $2d$  bands,  $\epsilon_{\pm}^{(\mu)}(k)$ , the band index  $\pm$  originating from the sublattice structure of the nanotube, and referring to bonding (valence) and anti-bonding (conduction) bands.

Within the tight binding scheme used here, these bands are associated with  $d$  independent one dimensional chains, each giving rise to one conduction and one valence band, and describing the motion of electrons with a given 'angular momentum'  $\mu$  (see Fig. 2(c)). Interestingly, each of these bands possesses a topological winding number [18]  $w^{(\mu)}$ . Non-zero winding numbers imply the presence of topologically protected end states [19, 37, 38]. Remarkably, we can express the total number of end states at each end of a semiconducting tube in a closed

form, just in terms of the nanotube's chirality,

$$N_{\text{edge}} = 2 \left\lfloor \frac{n-m}{3d} \right\rfloor + 3 \left\lfloor \frac{d+1}{3} \right\rfloor + 2\Theta(d) - \left( \left\lfloor \frac{d+1}{3} \right\rfloor + \Theta(d) \right) \Theta\left(\frac{n-m}{d}\right), \quad (5)$$

where  $\Theta(x) = (x+1) \bmod 3 - 1$  is a modified modulo function taking values 0 and  $\pm 1$ , and  $\lfloor \dots \rfloor$  denotes the floor function. In Fig. 2.(b), we display  $N_{\text{edge}}$  as a function of the chirality of the nanotubes. White squares indicate metallic tubes, while colored ones refer to semiconducting tubes. Clearly, most of the tubes are semiconducting, and the vast majority of semiconducting tubes possess topological end states, typically several ones. For zig-zag tubes with chirality  $(n, 0)$ , e.g., the number of end states increases linearly with the circumference of the tube,  $N_{\text{edge}}^{\text{zig-zag}} \approx n/3$ .

Remarkably, as our tight binding calculations also demonstrate, these end states are rather robust and not very sensitive to the form of the ending of the nanotube as long as it terminates in a minimal edge, i.e., with the minimal number of missing atoms and dangling bonds per period [39]. This is due to the fact that end states extend over many lattice sites, both along the circumference and along the width of the nanotube, hence defects at the end of the nanotube that break sublattice symmetry or the  $C_d$  symmetry mix end states only slightly. Note that end states are not robust against sublattice-selectively removing or adding some atoms at an end: this removes or creates end states, and alters the size and interaction of the end spins, accordingly. However, such modifications of the nanotube break the minimal edge condition, and are thus energetically unfavorable [39].

*Interacting nanotubes.*— To perform numerical calculations, we first construct a finite nanotube, and diagonalize the noninteracting part of the Hamiltonian Eq. (3) to find its eigenstates  $\phi_\alpha(\mathbf{r})$  and the corresponding eigenenergies,  $\epsilon_\alpha$ , and express the interaction term within this basis. Normal ordering needs to be treated with special care in this process. To treat nanotubes of reasonable length,  $L \approx 40$  nm, we restrict the many-body calculations to just about a hundred active states from the valence and conduction bands with energies  $|\epsilon_\alpha| < \Lambda \approx 5\Delta$ , with  $\Delta$  the band gap of the noninteracting infinite nanotube. Then we apply a density matrix renormalization group (DMRG) based approach adopted to Hamiltonians with arbitrary long-ranged two-body interactions [40–42] to determine the ground state and low lying excitations of the nanotube. In this procedure, we use  $U(1) \times U(1)$  symmetries, i.e. we fix the excess charge  $Q$  on the nanotube and the  $z$  component of the total spin,  $S_T^z$ . In practice, the computational basis is further optimized using fermionic mode transformation[43].

As sketched in Fig. 1, end spins manifest in the form of low energy sub-gap excitations, which can be described

by the effective Hamiltonian, Eq. (2). The many-body spectra observed reveal consistently the formation of end spins with  $S_{1,2} = N_{\text{edge}}/2$ , coupled to each other. In the absence of spin-orbit coupling, this interaction is  $SU(2)$  symmetrical, and the many-body spectrum consists of multiplets with total spin  $S_T = 0, \dots, N_{\text{edge}}$ .

The alignment and size of the electron spins at the ends of the nanotubes can be easily understood. In a topological nanotube,  $2N_{\text{edge}}$  spin degenerate states are split from the conduction and valence bands, and form the mid-gap states, and are therefore populated by  $2N_{\text{edge}}$  electrons in a neutral (half-filled) tube. End states are thus half-filled in a neutral nanotube. The spatial extension of these localized end states is roughly  $\xi_0 \sim \hbar c/\Delta \sim R$ , with  $c$  the Fermi velocity and  $R$  the radius of the nanotube. Electrons confined on these states interact therefore strongly with each other, and moving one electron from one end of the tube to the other would cost an energy  $\sim E_C \sim e^2/(\epsilon\xi_0) \sim e^2/(\epsilon R)$ . Therefore, to minimize their Coulomb energy,  $N_{\text{edge}}$  electrons go to each end of the tube. Moreover, since all these single particle levels are degenerate, and wave functions on one end overlap with each other, electrons at one end follow Hund's rule, and align their spins to mini-

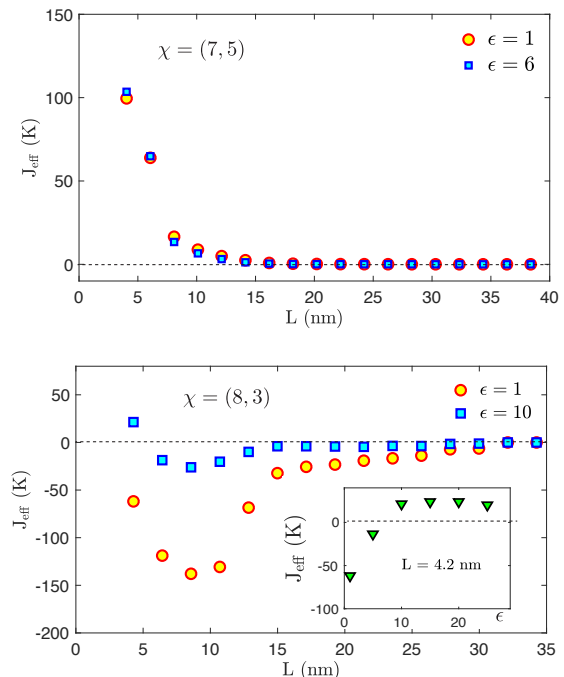


FIG. 3. Effective exchange interaction  $J_{\text{eff}}$  between the localized spins at the two ends of the nanotube as function of its length. When  $N_{\text{edge}}=1$ ,  $J_{\text{eff}}$  is always positive indicating an antiferromagnetic exchange, while for  $N_{\text{edge}} \geq 2$  an antiferromagnetic to ferromagnetic transition occurs. As the inset shows, for appropriate nanotube length, the sign of the interaction can be changed by changing the dielectric constant of the environment.

mize their interaction, thereby yielding a composite spin,  $S_{1,2} = N_{\text{edge}}/2$ , Eq. (1).

We have analyzed the excitation spectra of dozens of nanotubes, and verified Eq. (1) numerically in the presence of Coulomb interaction for all nanotubes listed in Fig. 2.b. In these simulations, we have observed end spins as large as  $S_{1,2} = 5/2$ , and corresponding ground state spins as large as  $S_T = S_1 + S_2 = 5$ . According to Eqs. (1) and (5), for appropriate chiralities and larger nanotube radii, the total emergent spin can largely exceed these values. The ground state spin of the nanotube is determined by the exchange coupling  $J_{\text{eff}}$  between the end spins. Being generated by tunneling between the topological end states, this coupling is expected to fall off exponentially with the length of the nanotube. The coupling  $J_{\text{eff}}$  can be readily extracted from the spin excitation spectrum, and is displayed for two particular nanotubes as a function of the nanotube length  $L$  in Fig. 3. On top, we show the results for a (7,5) nanotube with  $N_{\text{edge}} = 1$ , and corresponding spin  $S = 1/2$ 's at the edges. The coupling is antiferromagnetic, and therefore  $S_T = 0$  in this case, irrespective of the length of the nanotube. As expected, the coupling  $J_{\text{eff}}$  decays exponentially with  $L$ , reflecting the exponentially localized nature of the end states.

A completely different behavior is observed, however, for an (8,3) nanotube with  $N_{\text{edge}} = 2$ , as displayed on the bottom of Fig. 3. Here we observe an antiferromagnetic coupling in very short nanotubes with  $L \lesssim 5$  nm, while in longer tubes the interaction becomes ferromagnetic and decays exponentially, as expected.

The behavior shown in Figs. 3 appears to be generic. We have studied a great number of nanotubes with different chiralities, and in all nanotubes with  $N_{\text{edge}} = 1$  we find an antiferromagnetic coupling, while all nanotubes with  $N_{\text{edge}} \geq 2$  exhibit an exchange interaction that changes from antiferromagnetic to ferromagnetic with increasing nanotube length. As demonstrated in the lower panel, the precise location of the sign change is sensitive to the dielectric constant,  $\epsilon$ , and by appropriate engineering of  $\epsilon$ , one can even completely decouple the two end spins. This mechanism provides a tool to perform quantum manipulations with the end spins.

*Charging the end states.*— As discussed above, a topological nanotube behaves to a large extent as a self-organized double quantum dot system. Whether one can charge these topological quantum dots or not and observe the end states in a direct spectroscopic (tunneling) experiment, depends largely on screening, i.e., the value of  $\epsilon$ . Placing an additional electron to the topological states costs a Coulomb energy of the order of  $E_C \sim e^2/(\epsilon R)$ , while adding a delocalized particle to the valence band needs an energy  $\Delta \sim \hbar c/R$ . Therefore, for each chirality, there is a critical value  $\epsilon_C \sim e^2/(\hbar c)$  of the dielectric constant. For dielectric constants larger than  $\epsilon_C$  (strong screening), electrons and holes added to a neutral nanotube localize at the end and the topological quantum

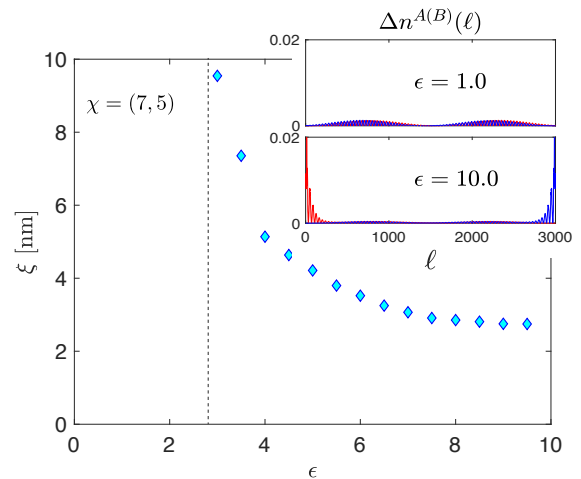


FIG. 4. Extension of the wave function of the additional spectrum, as a function of  $\epsilon$  in a (7,5) nanotube of length  $L = 30$  nm, with  $N_{\text{edge}} = 1$ . For  $\epsilon < \epsilon_C \approx 2.5$ , the added charge delocalizes along the nanotube, while for  $\epsilon > \epsilon_C$  the charge is added to the topological quantum dots (it is delocalized between them in the ground state). As the coloring indicates, the two end states live on different sublattices. The localization length of the added electron diverges as  $\epsilon$  approaches  $\epsilon_C$ .

dots can be charged, while for smaller dielectric constants (weak screening) they must go directly to the conduction or valence band, and delocalize along the nanotube.

According to our calculations, this transition happens at around  $\epsilon \approx 3$ , as is displayed in Fig. 4. The inset of Fig. 4 shows the spatial location of an electron added to the nanotube in terms of the position  $\ell$  along the helix. Clearly, the added particle is localized on sublattice  $A$  at one end, while it localizes on sublattice  $B$  at the other end (in close similarity with the SSH model). As shown in the main panel, the localization length of the added particle,  $\xi$  is strongly influenced by Coulomb interactions, and diverges as one approaches the critical value of  $\epsilon$ . This localization length should not be confused with that of the end spins, which remains of the order of  $R$ . Close to  $\epsilon \gtrsim \epsilon_C$ , the delocalized charges can create a glue between the end spins.

*Closing observations and conclusions.*— As we demonstrated in this work, most carbon nanotubes are topological, and all topological nanotubes possess interaction induced end spins, residing at the edges of the tube, and localized within a distance  $\sim \xi_0 \sim R$ . Being protected by topology, these naturally formed end spins are robust, are typically larger than spin  $S = 1/2$ , and couple to each other exponentially weakly in longer nanotubes (longer than a few nanometers). Their presence may provide a natural explanation for the intrinsic spin formation observed longtime ago in encapsulated nanotubes (pea pods) [44], and simple model calculations support that an exponentially weak ferromagnetic ex-

change quite naturally explains the super-Curie behavior reported earlier [45].

The large end spins demonstrated here are the nanotube analogues of ferromagnetic edge states appearing in graphene nanoribbons [24, 26–29, 46]. Indeed, selecting *any* topologically non-trivial chirality  $(p, q)$  with  $p$  and  $q$  being relative primes, we can think of nanoribbons of width  $W$  as nanotubes with chirality  $(n, m) \equiv (r p, r q)$  and length  $L = W$ , with  $r$  taken to infinity. In this limit, the length of the nanotube remains finite while its radius  $R$  is taken to infinity, thereby yielding nanoribbons closed into a cylinder. In this limit, the rotational symmetry  $C_{d \rightarrow \infty}$  yields a proliferation of topological end states, thus forming a dispersionless band that is subject to Stoner ferromagnetism. The sign change of  $J_{\text{eff}}$  observed has also its counterpart in nanoribbons: in close analogy with the sign change of  $J_{\text{eff}}$  observed here, the coupling between ferromagnetic edge states is observed to change sign, too, from being antiferromagnetic to ferromagnetic as a function of  $W$  [28].

Topological nanotubes spontaneously form double dot devices, which may provide a platform for quantum computation. As we demonstrated, local probes such as scanning tunneling microscopy (STM) can be used to observe these 'topological quantum dots', however, to charge them, the effective dielectric constants must be increased over some critical value. Therefore, rather than using suspended nanotubes, nanotubes layered over some tunable dielectrics would be the most promising candidates for a direct experimental observation by tunneling spectroscopy. Another way to detect these protected end states may be via local optical spectroscopy. Excitonic states, i.e. bound sub-gap electron-hole excitations have been observed by two-photon spectroscopy in bulk nanotubes [47, 48]. Charging the end states, and binding a charge carrier of opposite sign to it should create similar excitonic edge states. These edge excitons should have a binding energy clearly distinct from that of the bulk excitons, and may be detected by optically probing the edge of the nanotube in the infrared. Direct edge state  $\rightarrow$  valence or conduction band excitations should also be possibly detected well below the optical gap,  $E_g = 2\Delta$ .

*Acknowledgments.*— We thank Ferenc Simon, Christoph Strunk, Levente Tapasztó, and P. Nemes-Incze for insightful discussions. This work has been supported by the National Research, Development and Innovation Office (NKFIH) through Grant Nos. K119442 and K120569, through the Hungarian Quantum Technology National Excellence Program, project no. 2017-1.2.1-NKP-2017-00001, by the BME-Nanotechnology FIKP grant (BME FIKP-NAT), by the OTKA grant number FK 132146 and by the Romanian National Authority for Scientific Research and Innovation, UEFISCDI, under project no. PN-III-P4-ID-PCE-2016-0032. W.I. acknowledges support from KAKENHI Grants Nos. JP15K05118, JP15KK0147, JP18H04282. Ö.L. also

acknowledges financial support from the Alexander von Humboldt foundation.

Ö.L. acknowledges support from the Center for Scalable and Predictive Methods for Excitation and Correlated Phenomena (SPEC), funded by the Computational Chemical Sciences Program of the U.S. Department of Energy (DOE).

- 
- [1] M. Z. Hasan and C. L. Kane, *Rev. Mod. Phys.* **82**, 3045 (2010).
  - [2] X.-L. Qi and S.-C. Zhang, *Rev. Mod. Phys.* **83**, 1057 (2011).
  - [3] N. Xu, Y. Xu, and J. Zhu, *npj Quantum Materials* **2**, 51 (2017).
  - [4] W. P. Su, J. R. Schrieffer, and A. J. Heeger, *Phys. Rev. Lett.* **42**, 1698 (1979).
  - [5] L. Li, Z. Xu, and S. Chen, *Phys. Rev. B* **89**, 085111 (2014).
  - [6] E. J. Meier, F. A. An, and B. Gadway, *Nature Communications* **7**, 13986 (2016).
  - [7] J.-C. Charlier, X. Blase, and S. Roche, *Rev. Mod. Phys.* **79**, 677 (2007).
  - [8] P. Ayala, R. Arenal, A. Loiseau, A. Rubio, and T. Pichler, *Rev. Mod. Phys.* **82**, 1843 (2010).
  - [9] E. A. Laird, F. Kuemmeth, G. A. Steele, K. Grove-Rasmussen, J. Nygård, K. Flensberg, and L. P. Kouwenhoven, *Rev. Mod. Phys.* **87**, 703 (2015).
  - [10] A. Donarini, M. Niklas, M. Schafberger, N. Paradiso, C. Strunk, and M. Grifoni, *Nature Communications* **10**, 381 (2019).
  - [11] G. Hills, C. Lau, A. Wright, S. Fuller, M. D. Bishop, T. Srimani, P. Kanhaiya, R. Ho, A. Amer, Y. Stein, D. Murphy, Arvind, A. Chandrakasan, and M. M. Shulaker, *Nature* **572**, 595 (2019).
  - [12] I. Khivrich, A. A. Clerk, and S. Ilani, *Nature Nanotechnology* **14**, 161 (2019).
  - [13] I. Shapir, A. Hamo, S. Pecker, C. P. Moca, Ö. Legeza, G. Zarand, and S. Ilani, *Science* **364**, 870 (2019).
  - [14] M. Margańska, D. R. Schmid, A. Dirnauhner, P. L. Stiller, C. Strunk, M. Grifoni, and A. K. Hüttl, *Phys. Rev. Lett.* **122**, 086802 (2019).
  - [15] A. Graf, M. Held, Y. Zakharko, L. Tropic, M. C. Gather, and J. Zaumseil, *Nature Materials* **16**, 911 (2017).
  - [16] T. Hata, R. Delagrangé, T. Arakawa, S. Lee, R. Deblock, H. Bouchiat, K. Kobayashi, and M. Ferrier, *Phys. Rev. Lett.* **121**, 247703 (2018).
  - [17] Y. Efroni, S. Ilani, and E. Berg, *Phys. Rev. Lett.* **119**, 147704 (2017).
  - [18] W. Izumida, R. Okuyama, A. Yamakage, and R. Saito, *Phys. Rev. B* **93**, 195442 (2016).
  - [19] R. Okuyama, W. Izumida, and M. Eto, *Phys. Rev. B* **99**, 115409 (2019).
  - [20] Y. Higuchi, K. Kusakabe, N. Suzuki, S. Tsuneyuki, J. Yamauchi, K. Akagi, and Y. Yoshimoto, *Journal of Physics: Condensed Matter* **16**, S5689 (2004).
  - [21] O. Hod and G. E. Scuseria, *ACS Nano* **2**, 2243 (2008).
  - [22] H.-H. Lin, *Phys. Rev. B* **58**, 4963 (1998).
  - [23] A. Mañanes, F. Duque, A. Ayuela, M. J. López, and J. A. Alonso, *Phys. Rev. B* **78**, 035432 (2008).

- [24] J. Kunstmann, C. Özdoğan, A. Quandt, and H. Fehske, *Phys. Rev. B* **83**, 045414 (2011).
- [25] K. Wakabayashi, K. Sasaki, T. Nakanishi, and T. Enoki, *Science and Technology of Advanced Materials* **11**, 054504 (2010).
- [26] S. Dutta and K. Wakabayashi, *Scientific Reports* **2**, 519 (2012).
- [27] O. V. Yazyev, R. B. Capaz, and S. G. Louie, *Phys. Rev. B* **84**, 115406 (2011).
- [28] G. Z. Magda, X. Jin, I. Hagymási, P. Vancsó, Z. Osváth, P. Nemes-Incze, C. Hwang, L. P. Biró, and L. Tapasztó, *Nature* **514**, 608 (2014).
- [29] C. Tao, L. Jiao, O. V. Yazyev, Y.-C. Chen, J. Feng, X. Zhang, R. B. Capaz, J. M. Tour, A. Zettl, S. G. Louie, H. Dai, and M. F. Crommie, *Nature Physics* **7**, 616 (2011).
- [30] S. Reich, J. Maultzsch, C. Thomsen, and P. Ordejón, *Phys. Rev. B* **66**, 035412 (2002).
- [31] E. A. Laird, F. Kuemmeth, G. A. Steele, K. Grove-Rasmussen, J. Nygård, K. Flensberg, and L. P. Kouwenhoven, *Rev. Mod. Phys.* **87**, 703 (2015).
- [32] F. Kuemmeth, S. Ilani, D. C. Ralph, and P. L. McEuen, *Nature* **452**, 448 (2008).
- [33] V. Perebeinos, J. Tersoff, and P. Avouris, *Phys. Rev. Lett.* **92**, 257402 (2004).
- [34] C. T. White, D. H. Robertson, and J. W. Mintmire, *Phys. Rev. B* **47**, 5485 (1993).
- [35] R. A. Jishi, M. S. Dresselhaus, and G. Dresselhaus, *Phys. Rev. B* **47**, 16671 (1993).
- [36] See Supplementary material for details on the effective 1D lattice model and DMRG calculations which includes Refs. [30, 31, 33–35].
- [37] Y. Hatsugai, *Phys. Rev. Lett.* **71**, 3697 (1993).
- [38] J. C. Teo and C. L. Kane, *Physical Review B* **82**, 115120 (2010).
- [39] A. Akhmerov and C. Beenakker, *Physical Review B* **77**, 085423 (2008).
- [40] S. R. White, *Phys. Rev. Lett.* **77**, 3633 (1996).
- [41] U. Schollwöck, *Rev. Mod. Phys.* **77**, 259 (2005).
- [42] Ö. Legeza and J. Sólyom, *Phys. Rev. B* **68**, 195116 (2003).
- [43] C. Krumnow, L. Veis, Ö. Legeza, and J. Eisert, *Phys. Rev. Lett.* **117**, 210402 (2016).
- [44] F. Simon, H. Kuzmany, B. Náfrádi, T. Fehér, L. Forró, F. Fülöp, A. Jánossy, L. Korecz, A. Rockenbauer, F. Hauke, and A. Hirsch, *Phys. Rev. Lett.* **97**, 136801 (2006).
- [45] B. Náfrádi, N. M. Nemes, T. Fehér, L. Forró, Y. Kim, J. E. Fischer, D. E. Luzzi, F. Simon, and H. Kuzmany, *Phys. Stat. Sol. (b)* **243**, 3106 (2006).
- [46] I. Hagymási and O. Legeza, *Phys. Rev. B* **94**, 165147 (2016).
- [47] F. Wang, G. Dukovic, L. E. Brus, and T. F. Heinz, *Science* **308**, 838 (2005).
- [48] J. Maultzsch, R. Pomraenke, S. Reich, E. Chang, D. Prezzi, A. Ruini, E. Molinari, M. S. Strano, C. Thomsen, and C. Lienau, *Phys. Rev. B* **72**, 241402 (2005).

**SUPPLEMENTAL INFORMATION FOR  
"TOPOLOGICALLY PROTECTED,  
CORRELATED END SPIN FORMATION IN  
CARBON NANOTUBES"**

**Effective 1D lattice model**

In this section, we describe how to construct the effective Hamiltonian. Our starting point is the quadratic tight binding Hamiltonian describing the underlying graphene sheet

$$H_0 = - \sum_{\mathbf{x}, \mathbf{x}', s} t(\mathbf{x} - \mathbf{x}') c_s^\dagger(\mathbf{x}) c_s(\mathbf{x}'), \quad (6)$$

where  $c_s(\mathbf{x})$  denotes the annihilation operator of an electron at site  $\mathbf{x}$  and with spin  $s = \{\uparrow, \downarrow\}$ , while  $t(\mathbf{x} - \mathbf{x}')$  represents the hopping integral between lattice sites  $\mathbf{x}$  and  $\mathbf{x}'$ . In our calculations, we also include second nearest neighbor hoppings to account for curvature effects [30] (see Fig. 5(b)).

A single wall carbon nanotube is characterized by its chirality  $\chi = (n, m)$ , where  $n$  and  $m$  are integers. These specify the chirality vector,  $\mathbf{C}$ , and the helical vector,  $\mathbf{H}$ , as [34, 35]

$$\mathbf{C} = n \mathbf{a}_1 + m \mathbf{a}_2, \quad \mathbf{H} = p \mathbf{a}_1 + q \mathbf{a}_2. \quad (7)$$

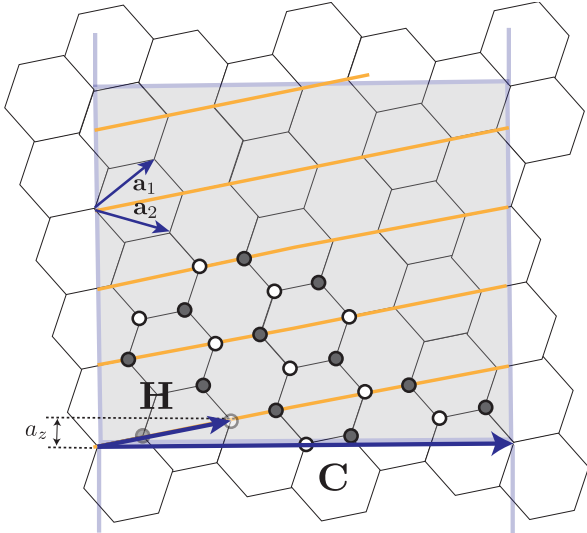


FIG. 5. Hexagonal lattice structure and helical labeling of atoms for a  $\chi = (4, 2)$  nanotube. The chirality vector  $\mathbf{C} = 4\mathbf{a}_1 + 2\mathbf{a}_2$  defines the direction, along which the nanotube is rolled up. Atoms aligned along the helicity vector,  $\mathbf{H} = \mathbf{a}_1 + \mathbf{a}_2$  form a helix, indicated by the orange line. The conventional unit cell is indicated as a gray rectangle, its vertical edge is given by  $\mathbf{T} = -4\mathbf{a}_1 + 5\mathbf{a}_2$ . Since  $d = \text{gcd}(n, m) = 2$  in this case, the vector  $\mathbf{C}/2$  brings the graphene sheet into itself, i.e., the  $(4, 2)$  nanotube possesses a  $C_2$  rotational symmetry. Correspondingly, one can make two helices of atoms  $A$  and two of atoms  $B$ .

Here  $p$  and  $q$  are two integers that satisfy the relation  $mp - nq = d$ , with  $d = \text{gcd}(n, m)$  the greatest common divisor of  $n$  and  $m$ .

The nanotube is obtained by rolling up a graphene sheet along  $\mathbf{C}$  (see Fig. 5). As explained in the main text, the rolled up tube is invariant under  $C_d$  rotations (corresponding to translations by a lattice vector  $\mathbf{C}/d$  of the graphene sheet) as well as under gliding rotations along the tube (generated by translations with  $\mathbf{H}$ ). As illustrated in Fig. 5, atoms forming the tube can correspondingly be organized into  $d$  helices of atoms  $A$  and  $d$  helices of atoms  $B$ .

Atoms on the nanotube are located at some physical positions  $\mathbf{r}$ . These positions can easily be expressed in terms of the atoms *original* position  $\mathbf{x}$  before the roll-up, expressed as

$$\mathbf{x} = \begin{cases} \frac{\nu}{d} \mathbf{C} + \ell \mathbf{H} & \text{if in } A, \\ \frac{\nu}{d} \mathbf{C} + \ell \mathbf{H} + \frac{\mathbf{a}_1 + \mathbf{a}_2}{3} & \text{if in } B, \end{cases} \quad (8)$$

with the integer  $\nu = \{0, 1, \dots, d-1\}$  specifying the helix, and  $\ell$  the location along this helix. Notice that periodic boundary conditions are used within the graphene plane, i.e., graphene atoms with coordinates  $\mathbf{x}$  and  $\mathbf{x} + \mathbf{C}$  are considered to be identical, and neighbors are identified accordingly. In our numerics, we use this helical construction, i.e., we specify atoms on the nanotube by the quantum numbers  $\nu, \ell$ , and the sublattice label  $\tau = A$  or  $B$ .

The integer label  $\ell$  can also be thought of as an indicator of the lattice position along the nanotube in units of

$$a_z = \frac{T}{N/d}, \quad (9)$$

which is the shortest distance between two consecutive atoms along one helix, as projected to the axial direction (see Fig. 5(b)). Here  $T = a\sqrt{3(n^2 + m^2 + nm)}/\text{gcd}(2n + m, 2m + n)$ , is the length of the translation vector (lattice constant) defining the conventional unit cell of the nanotube, and  $N = 2(n^2 + m^2 + nm)/d_R$  denotes the total number of  $A$  ( $B$ ) atoms in the conventional 1D nanotube unit cell [31].

Having constructed the positions  $\mathbf{r} = \mathbf{r}(\mathbf{x}) = \mathbf{r}(\nu, \ell, \tau)$ , as well as the tunneling matrix elements,  $t(\mathbf{r}, \mathbf{r}') = t(\mathbf{x} - \mathbf{x}')$ , we can construct and diagonalize the non-interacting part of the Hamiltonian (3) in the main text, and obtain the corresponding eigenfunctions  $\phi_\alpha(\mathbf{r}) \equiv \phi_\alpha(\nu, \ell, \tau)$ , and rewrite the noninteracting part of the Hamiltonian as

$$H_0 = \sum_{\alpha, s} \epsilon_\alpha c_{\alpha s}^\dagger c_{\alpha s}. \quad (10)$$

Next, we express the interaction in this basis as

$$H_{\text{int}} = \frac{1}{2} \sum_{s_1 s_2} \sum_{\alpha \beta \gamma \delta} V_{\alpha \beta; \gamma \delta} c_{\alpha s_1}^\dagger c_{\gamma s_2}^\dagger c_{\delta s_2} c_{\beta s_1} + \sum_s \sum_{\alpha, \beta, \eta} \left( V_{\alpha \eta; \eta \beta} c_{\alpha s}^\dagger c_{\beta s} - V_{\alpha \beta; \eta \eta} c_{\alpha s}^\dagger c_{\beta s} \right), \quad (11)$$

where the last terms originate from normal ordering, and  $V_{\alpha \beta; \gamma \delta}$  denotes the two-body interaction element,

$$V_{\alpha \beta; \gamma \delta} = \sum_{a, a'} \phi_\alpha^*(a) \phi_\beta(a) V(\mathbf{r}_a - \mathbf{r}_{a'}) \phi_\gamma^*(a') \phi_\delta(a'). \quad (12)$$

Here, for compactness, we have introduced the composite label,  $a = (\nu, \ell, \tau)$ . For effective Coulomb interaction we use the so-called Ohno potential [33],

$$V(\mathbf{r}_1 - \mathbf{r}_2) = \frac{e^2}{\epsilon_r} \frac{1}{\sqrt{(\mathbf{r}_1 - \mathbf{r}_2)^2 + \alpha^2}},$$

with  $\alpha = \frac{e^2}{\epsilon U_0}$ , and  $U_0 = 11.3$  eV for the  $\pi$ -orbital [33].

To perform density matrix renormalization group (DMRG) calculations, we now assume that quantum fluctuations only influence the occupation of levels not far from the Fermi energy, and therefore restrict the active space of our many-body computations to states close to the Fermi energy,  $|\epsilon_\alpha| < \Lambda$ , with  $\Lambda$  an energy cut-off introduced. However, in doing so, we must treat occupied 'core' levels and normal ordering carefully. In practice, we do that by adding the truncated normal ordered part of the interactions to the kinetic energy, and thereby renormalizing the non-interacting part as

$$H_0 \rightarrow \tilde{H}_0 \equiv \sum_s \sum_{|\epsilon_\alpha|, |\epsilon_\beta| < \Lambda} T_{\alpha \beta} c_{\alpha s}^\dagger c_{\beta s}, \quad (13)$$

with the single particle matrix elements defined as

$$T_{\alpha \beta} = \epsilon_\alpha \delta_{\alpha \beta} + \sum_{|e_\gamma| < \Lambda} \left( V_{\alpha \gamma; \gamma \beta} - V_{\alpha \beta; \gamma \gamma} \right), \quad (14)$$

while interactions are restricted to active orbitals,

$$H_{\text{int}} \rightarrow \tilde{H}_{\text{int}} \equiv \frac{1}{2} \sum_{s_1 s_2} \sum_{\alpha, \beta, \gamma, \delta} V_{\alpha \beta; \gamma \delta} c_{\alpha s_1}^\dagger c_{\gamma s_2}^\dagger c_{\delta s_2} c_{\beta s_1}. \quad (15)$$

Here the tilde sign indicates restriction to active orbitals. A delicate and important feature of the cut-off construction above is that it *preserves* electron-hole symmetry even for the interacting spectrum, in case we have only nearest neighbor hopping, as readily verified by explicit analytical calculations as well as by our numerics.

### DMRG calculations with long range Coulomb interactions

For our DMRG calculations we employ the two-site

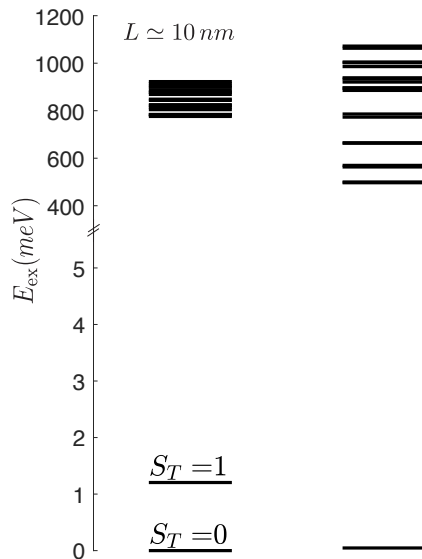


FIG. 6. Energy excitation spectrum of a nanotube in the  $S_T^z = 0$  sector, as obtained with the DMRG. The chirality of the nanotube is  $(n, m) = (7, 5)$  and  $L \simeq 10$  nm. The left columns represent the many body spectrum while the right column represent the non-interacting spectrum. On the left side, the energy separation between the ground state and the first excited state have been magnified 20 times, for better visibility. The numbers on the two levels are the values of the total spins  $S_T$  as extracted from the DMRG calculations.

variant of DMRG, as first introduced by White [40]. We compute the ground state energy as well as the energy of a few excited states above the ground state. In practice, the performance of the DMRG can be boosted significantly by optimizing the computational basis using fermionic mode transformation [43].

The local electron density for the effective 1D lattice model is then easily expressed in terms of the reduced (spin traced) density matrix  $\varrho_{\alpha \beta} \equiv \sum_s \langle c_{\alpha s}^\dagger c_{\beta s} \rangle$  as

$$n(\nu \ell \tau) = \sum_{\alpha \beta} \varrho_{\alpha \beta} \phi_\alpha^*(\nu \ell \tau) \phi_\beta(\nu \ell \tau) + n^{\text{core}}(\nu \ell \tau),$$

with  $n^{\text{core}}(\nu \ell \tau)$  the electron charge of the completely occupied core states. A summation over the helix label  $\nu$  yields the total density of atoms  $A$  or  $B$  at a helix position  $\ell$ ,

$$n^\tau(\ell) \equiv \sum_\nu n(\nu \ell \tau). \quad (16)$$

Computing then the excess charge density,  $\Delta n^\tau(\ell) \equiv n_{Q=1}^\tau(\ell) - n_{Q=0}^\tau(\ell)$ , induced upon adding one electron to the nanotube, allows us, for example, to explore the localization and spin structure of the edge states and to estimate their extension in real space, as presented in Fig. 4 of the main text. In Fig. 6 we represent the lowest part of the energy spectrum for a nanotube with chirality  $(n, m) = (7, 5)$ . It allows us to extract the exchange



interaction between the localized spins at the two ends of the nanotube. For (7,5) chirality, the ground state is antiferromagnetic with a total spin  $S_T = 0$ . In general, two spins of size  $S$ , coupled by the Hamiltonian (2), has an spectrum  $E_n = J_{\text{eff}}(S_T(S_T + 1) - 2S(S + 1))/2$ .

The energy difference between the first excited state ( $S_T = 1$ ) and the ground state ( $S_T = 0$ ) is therefore  $\Delta E = J_{\text{eff}}$ , which allows us to extract  $J_{\text{eff}}$  directly from the DMRG spectrum. In case of larger end spins, further low-lying excitations appear with energies, which we can also clearly see in the spectrum.